Mechanical properties and deformation behavior of Zr-based bulk metallic glass composites reinforced with tungsten fibers or tungsten powders

Zhen Zhang[1, 2], Jin-he Wang[2], Zheng-kun Li[3], *Hua-meng Fu[2], Hong Li[3], Zheng-wang Zhu[3], and Hai-feng Zhang[2, 3]

1. School of Materials Science and Engineering, Shenyang University of Technology, Shenyang 110870, China

2. Shi-changxu Innovation Center for Advanced Materials, Institute of Metal Research, Chinese Academy of Sciences, Shenyang110016, China

3. School of Metallurgy, Northeastern University, Shenyang 110004, China

Abstract: The tungsten fibers or powders reinforced $Zr_{52}Cu_{32}Ni_6Al_{10}$, $(Zr_{52}Cu_{32}Ni_6Al_{10})_{98}Nb_2$, and $(Zr_{52}Cu_{32}Ni_6Al_{10})_{98}Be_2$ bulk metallic glass composites (BMGCs) were fabricated using the infiltration casting method. In this study, the wettability between the amorphous alloy melts and tungsten substrates was investigated using the sessile drop method, revealing excellent wettability at 1,010 °C. Consequently, an infiltration temperature of 1,010 °C was chosen for composite material fabrication. Structural characterization and mechanical property test of both composites were conducted through scanning electron microscopy (SEM), and X-ray diffraction (XRD), and universal mechanical testing. Both tungsten fiber or tungsten powder reinforced $Zr_{52}Cu_{32}Ni_6Al_{10}$ and $(Zr_{52}Cu_{32}Ni_6Al_{10})_{98}Be_2$ composites exhibit the formation of W-Zr phase. In contrast, the tungsten fiber or tungsten powder reinforced $(Zr_{52}Cu_{32}Ni_6Al_{10})_{98}Nb_2$ composites does not show the formation of W-Zr phase. X-ray diffraction patterns confirm the presence of W reinforcement phases in both composites. The successful fabrication of both composites is evidenced by their remarkable mechanical properties under room temperature compression. The yield strength of all the three tungsten fiber-reinforced composite sample exceeds 2,400 MPa, with the plastic strain exceeding 3.9%, while the yield strength of all the three tungsten powder-reinforced composite sample surpasses 2,700 MPa, with the plastic strain exceeding 30%. Fracture analysis reveals longitudinal splitting in the tungsten fiber-reinforced composites, contrasting with brittle fracture in the tungsten powder-reinforced composites. The denser the shear bands on the amorphous matrix of the two types of composite materials, the better their mechanical properties.

Keywords: Zr-based BMGCs; shear bands; fracture mode; compression mechanical properties; wettability

CLC numbers: TG146.4⁺14   **Document code:** A

1 Introduction

Despite the numerous outstanding properties exhibited by amorphous alloys, their shear fracture mode and nearly zero plasticity at room temperature greatly limits their application range as engineering materials [1-4]. This is because plastic deformation in metallic glasses is concentrated in narrow shear bands, which subsequently undergo rapid propagation, leading to catastrophic failure characterized by a lack of plasticity [5-8].

To enhance the plasticity of bulk metallic glasses (BMGs),

extensive research has been conducted by scientists and researchers both domestically and internationally. Numerous endeavors have been concentrated on enhancing the ductility of bulk metallic glasses through the fabrication of composite materials with BMGs matrix [9]. To date, there are two types of bulk metallic glass composites, known as intrinsic and extrinsic composites, which involve the in-situ formation or/and ex-situ addition of crystalline phases [10, 11]. Both types of BMGCs aim to enhance the plasticity of BMGs by impeding shear band propagation within BMGs and facilitating the rapid expansion of multiple shear bands [12, 13].

In the case of ex-situ phase-reinforced BMGCs, a second phase preform is initially positioned within a mold, and subsequently, the molten BMGs are infiltrated into the preform. Among the ex-situ added crystalline phases, fibers and powders are considered

*Hua-meng Fu

Male, born in 1976, Ph. D., Professor. His research interests mainly focus on amorphous alloys and their composites.

E-mail: hmfu@imr.ac.cn

the foremost reinforcements. Fiber-reinforced composites typically exhibit anisotropic characteristics, while powder-reinforced composites generally demonstrate isotropic properties [14, 15].

A large number of researchers have extensively studied the mechanical properties, deformation, and fracture behavior of fiber-reinforced composites and powder-reinforced composites, owing to their exceptional performance. It has discovered that composites reinforced with tungsten materials (tungsten fibers, tungsten powders) demonstrate superior performance, attributed to the excellent wettability between tungsten materials and the metallic glass matrix. The introduction of fiber reinforcement in composites not only affects the mechanical properties of the metallic glass matrix, but also alters the fracture process and fracture mode of the matrix [16, 17]. Moreover, the incorporation of powders in composites significantly enhances the mechanical properties of the metallic glass matrix and can modify the fracture process, while maintaining the same fracture mode as the metallic glass matrix [18].

In this study, $Zr_{52}Cu_{32}Ni_6Al_{10}$, $(Zr_{52}Cu_{32}Ni_6Al_{10})_{98}Nb_2$, and $(Zr_{52}Cu_{32}Ni_6Al_{10})_{98}Be_2$ were chosen as the amorphous alloy matrix due to their strong amorphous-forming ability and relatively simple fabrication process in the Zr-Cu-Ni-Al system. The tungsten fiber or powder-reinforced amorphous composite materials were prepared using the infiltration casting method, aiming to overcome traditional drawbacks of amorphous alloys, such as high susceptibility to shear fracture and near-zero plasticity at room temperature. This study provides a theoretical basis for preparation of tungsten-reinforced amorphous composite materials, including morphology of the reinforcing phase, and types of the reinforcing phases and amorphous matrix.

2 Experimental

$Zr_{52}Cu_{32}Ni_6Al_{10}$, $(Zr_{52}Cu_{32}Ni_6Al_{10})_{98}Nb_2$, and $(Zr_{52}Cu_{32}Ni_6Al_{10})_{98}Be_2$ were prepared by arc melting the mixture of Zr, Cu, Ni, Al, Nb and Be elements (purity over 99.8%) in a Ti-gettered high-purity argon atmosphere. In order to achieve a homogeneous mixture of all components within the alloy, each alloy ingot was remelted four times [19]. Before preparing the composite materials, it is necessary to conduct ultra-high vacuum wetting tests between the three types of amorphous alloys and tungsten substrates to determine their wetting behavior. In this study, the sessile drop method was employed for the wetting testing. After conducting the wetting test experiments, each alloy ingot was crushed and then placed into the equipment used for preparing the composite materials. Both types of composites were fabricated using the infiltration casting method. Under high temperature and high vacuum conditions, they were individually infiltrated into the tungsten fibers and tungsten powders, resulting in the formation of the two types of composite materials [20].

The added tungsten fibers (with a diameter of 200 μm) accounted for 83% of the total composite volume, while the

added tungsten powder (with a size range of 60–120 μm) accounted for 55% of the total composite volume. Composite material rods (Φ20 mm×100 mm) were prepared into room temperature quasi-static compression samples with a diameter of 4 mm and a height of 8 mm through wire-cut electrical discharge machining (EDM). Furthermore, some samples were longitudinally bisected along the diameter to investigate the propagation of shear bands on the side of the composite material. The two end faces of the compression samples were polished using #2000 sandpaper, ensuring parallelism between them and perpendicular to the sample's lateral sides. Compression at room temperature was performed using an AG-I 500 kN compression machine, with a compression rate of $2.4×10^{-1}$ mm·min^{-1}. Each sample was subjected to three repeated experiments to minimize the impact of experimental errors. After the compression experiments, the samples were ultrasonically cleaned with anhydrous ethanol. Subsequently, the fracture morphology and the morphology of the shear bands on the side were characterized using scanning electron microscopy (SEM, MIRA3-LMH). Moreover, thin slices with a thickness of 1 mm were cut vertically from the composite material rod. After grinding with sandpaper, the structure and phases of the composite material were characterized using the X-ray diffractometer (XRD, Rigaku D/max 2,400), with the scanning range set from 10° to 100° and a scanning speed of 4°·min^{-1}.

3 Results and discussion

3.1 Wettability between amorphous alloy melt and tungsten substrate

The wettability between three types of amorphous alloy melts and tungsten substrates at 930 °C, 970 °C and 1,010 °C, respectively is shown in Fig. 1.

According to Fig. 1, it can be concluded that the contact angles of the three types of amorphous alloy melts on tungsten substrates gradually decrease with increasing heating temperature. Furthermore, when heated to 1,010 °C, the contact angles of the three types of amorphous alloy melts on tungsten substrates reach their minimum values, indicating the best wettability at this temperature. At this temperature, the $(Zr_{52}Cu_{32}Ni_6Al_{10})_{98}Be_2$ exhibits the best wettability with the tungsten substrate, while the difference in wettability between $(Zr_{52}Cu_{32}Ni_6Al_{10})_{98}Nb_2$ and $Zr_{52}Cu_{32}Ni_6Al_{10}$ with the tungsten substrates is negligible.

3.2 Microstructure of tungsten fibers or tungsten powders reinforced amorphous composite material

Figures 2 and 3 depict the SEM images of the cross-section of tungsten fiber or tungsten powder reinforced amorphous composite materials. In this study, the notation $Wf/Zr_{52}Cu_{32}Ni_6Al_{10}$, $Wf/(Zr_{52}Cu_{32}Ni_6Al_{10})_{98}Nb_2$ and $Wf/(Zr_{52}Cu_{32}Ni_6Al_{10})_{98}Be_2$ were utilized to designate three varieties of amorphous composites reinforced with tungsten fibers, while $Wp/Zr_{52}Cu_{32}Ni_6Al_{10}$, $Wp/(Zr_{52}Cu_{32}Ni_6Al_{10})_{98}Nb_2$ and Wp/
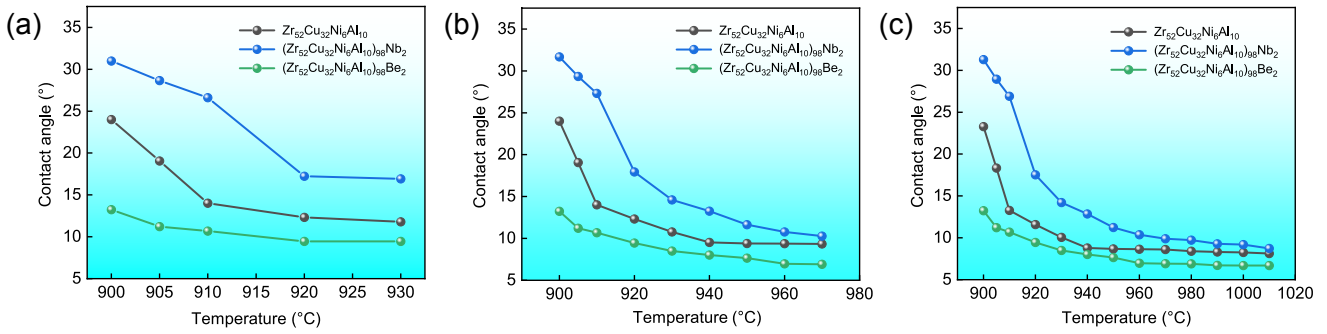
Fig. 1: Variation of contact angles of three types of amorphous alloy melts on tungsten substrates at 930 °C (a), 970 °C (b) and 1,010 °C (c)
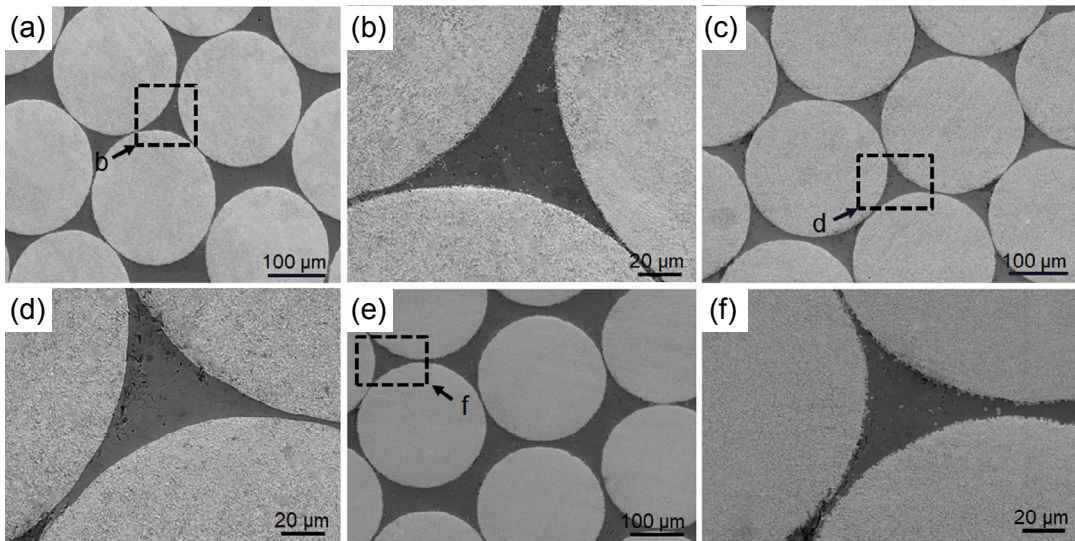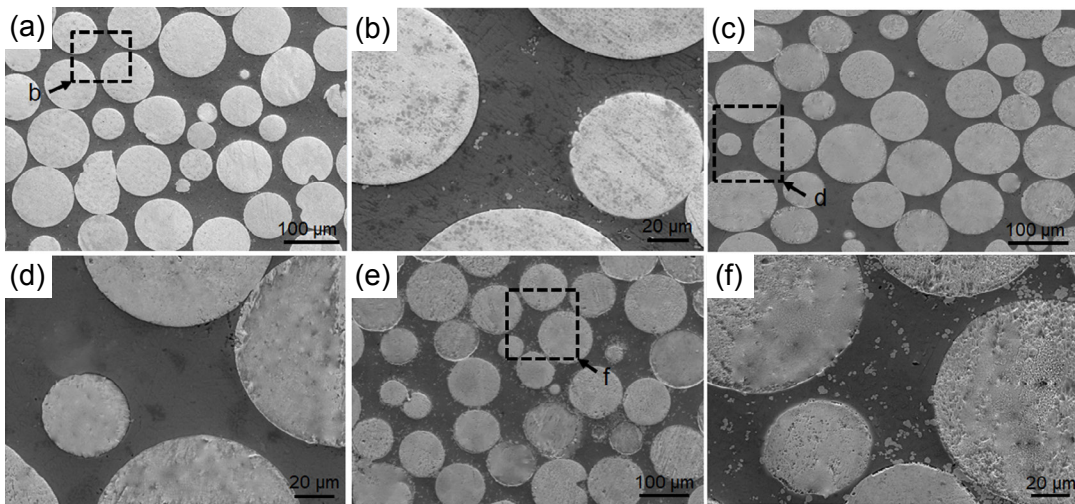

Fig. 2: Microstructure of cross-section of tungsten fiber reinforced amorphous composite materials: (a)–(b) Wf/$Zr_{52}Cu_{32}Ni_6Al_{10}$; (c)–(d) Wf/$(Zr_{52}Cu_{32}Ni_6Al_{10})_{98}Nb_2$; (e)–(f) Wf/$(Zr_{52}Cu_{32}Ni_6Al_{10})_{98}Be_2$

Fig. 3: Microstructure of the cross-section of tungsten powder reinforced amorphous composite materials: (a)–(b) Wp/$Zr_{52}Cu_{32}Ni_6Al_{10}$; (c)–(d) Wp/$(Zr_{52}Cu_{32}Ni_6Al_{10})_{98}Nb_2$; (e)–(f) Wp/$(Zr_{52}Cu_{32}Ni_6Al_{10})_{98}Be_2$

$(Zr_{52}Cu_{32}Ni_6Al_{10})_{98}Be_2$ were used to indicate three varieties of amorphous composites reinforced with tungsten powders.

Based on Figs. 2 and 3, it is evident that there is a favorable interface bonding between the matrix and the reinforcing phase in both types of composite materials. Additionally, melting or cracking of tungsten fibers or tungsten powders is not observed.

From Figs. 2(a), (b), (e) and (f) and Figs. 3(a), (b), (e) and (f), it can be observed that the appearance of gray precipitates is evident on both amorphous matrices in $Zr_{52}Cu_{32}Ni_6Al_{10}$ and $(Zr_{52}Cu_{32}Ni_6Al_{10})_{98}Be_2$. However, from Figs. 2(c) and (d) and Figs. 3(c) and (d), it can be seen that there is no occurrence of gray precipitates on amorphous matrix $(Zr_{52}Cu_{32}Ni_6Al_{10})_{98}Nb_2$.

The occurrence of gray precipitates can be attributed to the powerful interaction energy between the Zr element in the amorphous alloy and the W element in tungsten fibers or powder. More specifically, the Zr element exhibits a higher reactivity with the W element, resulting in the formation of precipitates known as W-Zr phase [21]. The absence of gray precipitates can be attributed to the addition of Nb element in the amorphous matrix of $(Zr_{52}Cu_{32}Ni_6Al_{10})_{98}Nb_2$. Furthermore, the interaction energy between Nb element and W element is greater than that between Zr element and W element [22]. Hence, Nb element preferentially segregates on tungsten fibers or tungsten powder, hindering the reaction of Zr element with W element, preventing them from forming the W-Zr phase [23].

3.3 X-ray diffraction analysis of amorphous composites reinforced with tungsten fibers or powders

Figure 4 displays the XRD patterns of the amorphous composite material reinforced with tungsten fibers or tungsten powders.

From Fig. 4, it can be observed that both Figs. 4(a) and (b) exhibit sharp diffraction peaks corresponding to the W

reinforcing phase in the XRD patterns. However, the positions of the W reinforcing phase differ between the two types of composite materials. In the tungsten fiber-reinforced amorphous composite material, the W reinforcing phase appears at 38° and 87°. In contrast, in the tungsten powder-reinforced amorphous composite material, the W reinforcing phase appears at 42°, 58°, 73° and 86°. Meanwhile, it can also be inferred from Figs. 4(a) and (b) that besides the diffraction peaks of the W strengthening phase in the XRD spectrum, there are also diffraction peaks of the W_2Zr phase, namely the W-Zr phase, as well as some peaks originating from partial crystallization of the amorphous matrix.

The volume fraction of tungsten fibers (83%) leads to the dominance of tungsten crystal diffraction peaks, overshadowing the broad scattering peaks of the amorphous matrix in the XRD patterns. Conversely, in the case of tungsten powder-reinforced amorphous composite material, the lower volume fraction of tungsten powder (55%) reduces the extent of overshadowing by tungsten crystal diffraction peaks. These two factors account for the distinctive observations seen in Figs. 4(a) and (b).
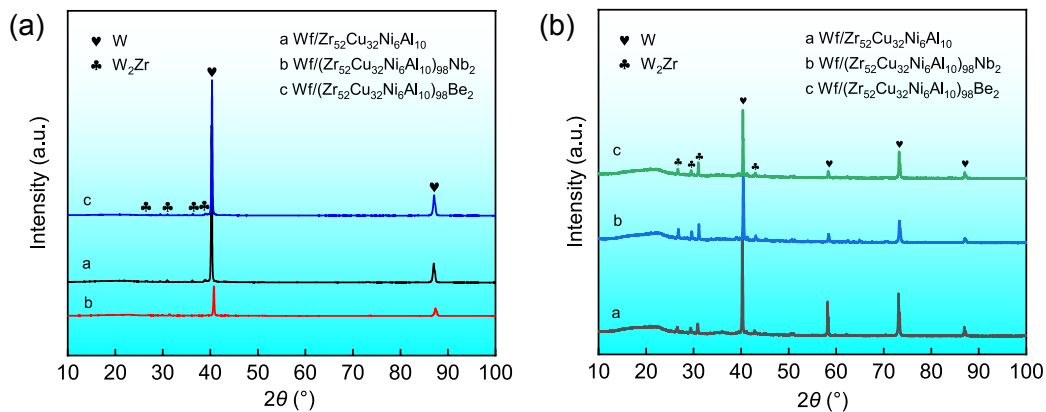

Fig. 4: XRD patterns of two types of composites: (a) tungsten fiber-reinforced composites; (b) tungsten power-reinforced composites
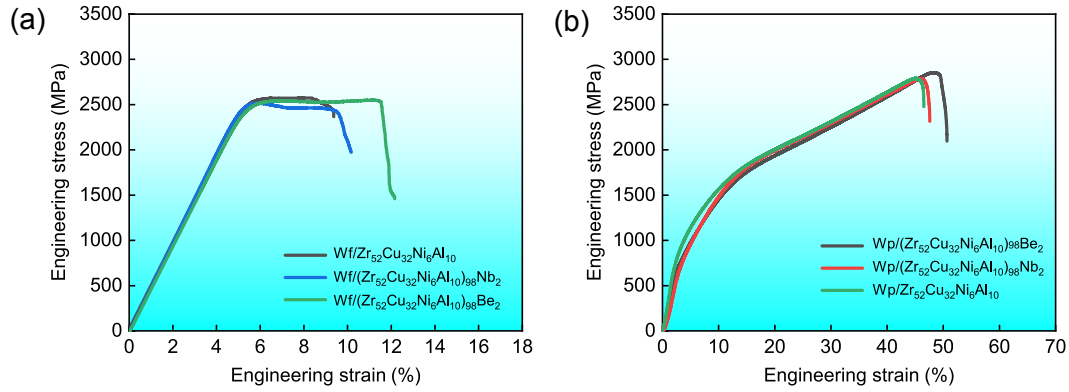
3.4 Compressive mechanical properties of tungsten fiber or tungsten powder reinforced amorphous composites

Figure 5 represents the compressive mechanical properties of tungsten fiber or tungsten powder reinforced amorphous composites. The various mechanical performance data of the two types of composite materials are shown in Table 1.

It can be observed from Fig. 5 and Table 1 that both types of composites significantly enhance the mechanical properties of the amorphous alloy matrix. Furthermore, the improvement in the mechanical properties of the amorphous alloy matrix is more pronounced in the case of tungsten powder reinforced amorphous composites. This indicates that the morphology of the reinforcing phase has a significant impact on the mechanical properties of the composite materials [24]. Tungsten powders reinforced amorphous composites demonstrate enhanced mechanical properties due to the introduction of

tungsten powder, which leads to the segmentation of the amorphous matrix into multiple regions (Figs. 3 and 10). Consequently, the presence of tungsten powders enhances resistance to the shear bands on the amorphous matrix during deformation under load.

By analyzing Fig. 5, a similar trend can be observed. Both tungsten fiber and tungsten powder reinforced $(Zr_{52}Cu_{32}Ni_6Al_{10})_{98}Be_2$ composites exhibit the best mechanical properties among the same type of composites. The fracture strength of this composite material reaches 2,835.4 MPa, and its plasticity achieves 34.3%. Additionally, tungsten fiber or tungsten powder reinforced $Zr_{52}Cu_{32}Ni_6Al_{10}$ and $(Zr_{52}Cu_{32}Ni_6Al_{10})_{98}Nb_2$ composites demonstrate similar mechanical properties within their respective groups. This is due to the difference in wettability between the amorphous matrix and the tungsten reinforcing phase is very small. Only good wettability can ensure a strong interface

Fig. 5: Compressive mechanical properties of tungsten fiber or tungsten powder reinforced amorphous composites: (a) tungsten fiber-reinforced composites; (b) tungsten power-reinforced composites

Table 1: Mechanical performance data of the two types of composite material

Composite materials	Fracture strength (MPa)	Max strain (%)	Plasticity (%)
$Wf/Zr_{52}Cu_{32}Ni_6Al_{10}$	2,437.2	9.3	3.9
$Wf/(Zr_{52}Cu_{32}Ni_6Al_{10})_{98}Nb_2$	2,430.3	9.5	4.2
$Wf/(Zr_{52}Cu_{32}Ni_6Al_{10})_{98}Be_2$	2,531.9	12.1	6.5
$Wp/Zr_{52}Cu_{32}Ni_6Al_{10}$	2,785.9	45.9	31.0
$Wp/(Zr_{52}Cu_{32}Ni_6Al_{10})_{98}Nb_2$	2,783.6	46.4	31.6
$Wp/(Zr_{52}Cu_{32}Ni_6Al_{10})_{98}Be_2$	2,835.4	49.2	34.3

bonding between the matrix and the reinforcing phase, leading to better load transfer and stress distribution, thus avoiding stress concentration. Therefore, the wettability has a significant impact on the mechanical properties of composite materials. According to the results obtained from the wettability experiments in this study, it can be inferred that at 1,010 °C, $(Zr_{52}Cu_{32}Ni_6Al_{10})_{98}Be_2$ demonstrates superior wetting behavior with tungsten, whereas $Zr_{52}Cu_{32}Ni_6Al_{10}$ and $(Zr_{52}Cu_{32}Ni_6Al_{10})_{98}Nb_2$ exhibit comparable wettability with tungsten. This variation in wettability explains the observed trends in the mechanical data for this particular group.
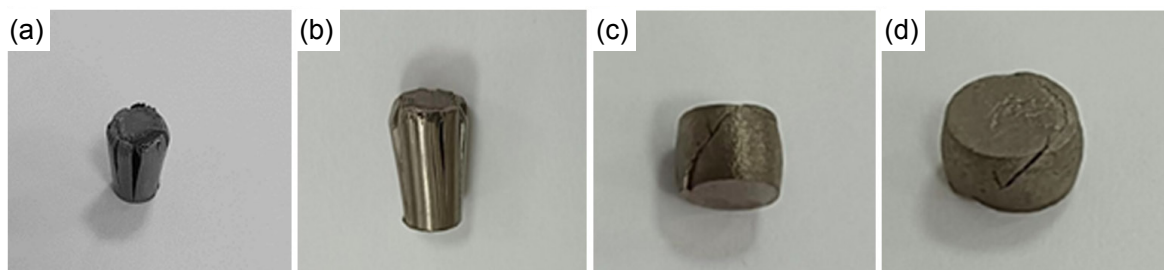
3.5 Fracture analysis of amorphous composites reinforced with tungsten fibers or powders

Figure 6 illustrates the upright and side view of the compressed samples of the amorphous composite materials reinforced with tungsten fibers and powders, respectively.

From Fig. 6, it can be observed that the amorphous composite material reinforced with tungsten fibers not only changes the fracture process of the amorphous alloy matrix but also alters its fracture mode.

Figures 7 and 8 display the microstructural morphology of the fracture surface of the amorphous composite material reinforced with tungsten fibers or tungsten powders, respectively.

According to Fig. 7, it can be observed that the composites reinforced with tungsten fibers exhibit a longitudinal cleavage fracture mode. This longitudinal cleavage fracture mode can be further classified into two types. One type is the mode where the fracture propagates through the tungsten fibers, and the other type is the mode where the fracture occurs along the amorphous matrix [25]. Significant loads are borne by the tungsten fibers, leading to their fracture and penetration when the external stress mainly concentrates on them. The occurrence of the fracture along the amorphous matrix mode

Fig. 6: Fracture analysis of amorphous composites: (a)–(b) tungsten fiber-reinforced composites; (c)–(d) tungsten power-reinforced composites
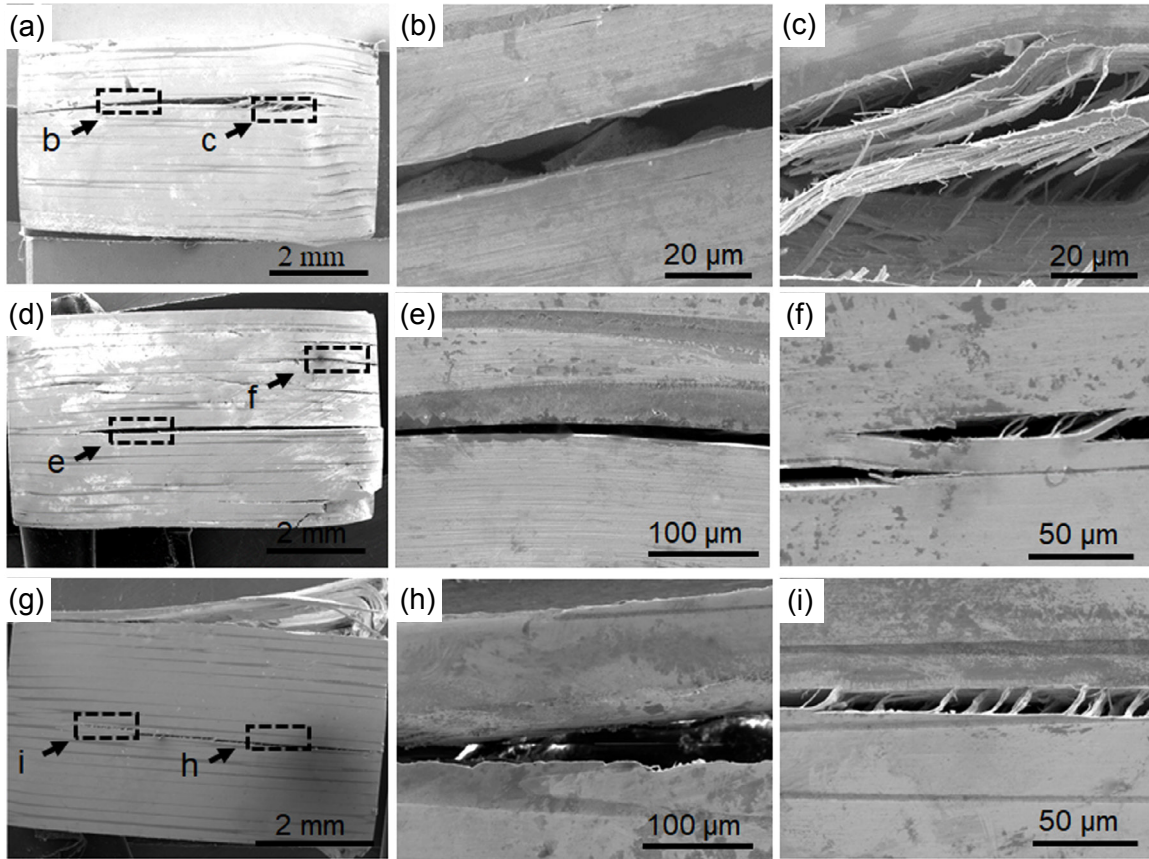
Fig. 7: Morphologies of fracture surface of tungsten fiber-reinforced amorphous composite materials: (a)–(c) Wf/$Zr_{52}Cu_{32}Ni_6Al_{10}$; (d)–(f) Wf/$(Zr_{52}Cu_{32}Ni_6Al_{10})_{98}Nb_2$; (g)–(i) Wf/$(Zr_{52}Cu_{32}Ni_6Al_{10})_{98}Be_2$
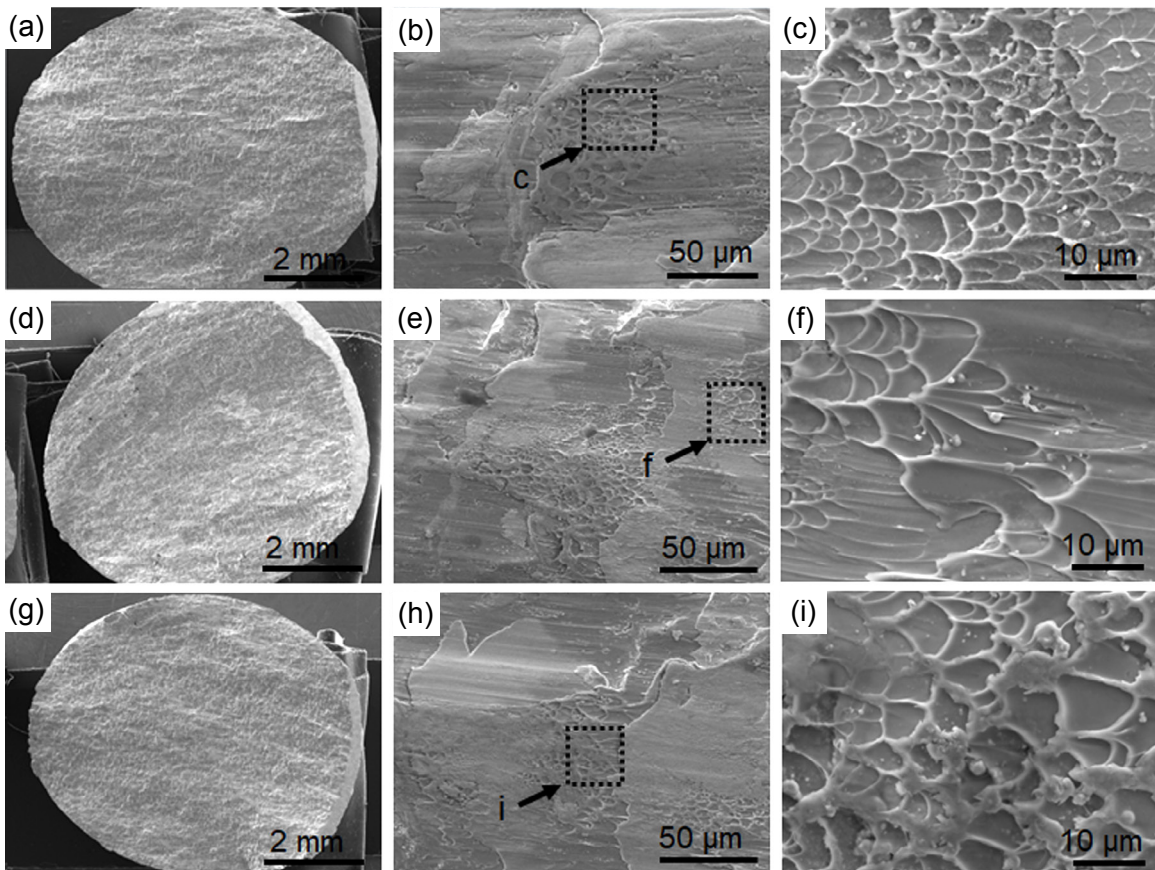

Fig. 8: Morphologies of fracture surface of tungsten powder-reinforced amorphous composite materials: (a)–(c) Wp/$Zr_{52}Cu_{32}Ni_6Al_{10}$; (d)–(f) Wp/$(Zr_{52}Cu_{32}Ni_6Al_{10})_{98}Nb_2$; (g)–(i) Wp/$(Zr_{52}Cu_{32}Ni_6Al_{10})_{98}Be_2$

is due to the fact that, despite experiencing high stress, the tungsten fibers can have stress bypass them, leading to the stress primarily acting upon the amorphous matrix or interface. Consequently, fracture along the amorphous matrix or interface debonding phenomenon occurs.

Based on the observation from Fig. 8, it is evident that the fracture surfaces of the tungsten powder-reinforced amorphous composite material exhibit a smooth appearance with distinct vein-like patterns, indicating a shear fracture. These patterns are attributed to the shear stress exerted during the fracture process. From Fig. 8, it can also be observed that there are small amounts of droplets present on the vein-like patterns. This is due to the generation of significant heat during the room temperature compression process of this type of composite material, leading to partial crystallization of the amorphous matrix and subsequent re-melting [26]. As a result, a small number of droplets form on the vein-like patterns. In addition, these droplets hinder partial expansion of the vein-like patterns, resulting in a smoother and more even surface in that particular region.

3.6 Shear band analysis of amorphous composites reinforced with tungsten fibers or powders

Figures 9 and 10 show the morphology of the shear bands on the side surfaces of the tungsten fiber-reinforced and tungsten powder-reinforced amorphous composite materials, respectively.

From Figs. 9 and 10, it can be observed that the shear bands on the amorphous matrix $(Zr_{52}Cu_{32}Ni_6Al_{10})_{98}Be_2$ are the most

densely distributed, while the density of shear bands on the amorphous matrices $Zr_{52}Cu_{32}Ni_6Al_{10}$ and $(Zr_{52}Cu_{32}Ni_6Al_{10})_{98}Nb_2$ are relatively similar. As mentioned earlier, Wf/$(Zr_{52}Cu_{32}Ni_6Al_{10})_{98}Be_2$ and Wp/$(Zr_{52}Cu_{32}Ni_6Al_{10})_{98}Be_2$ exhibit the best mechanical properties among their counterparts. Wf/$Zr_{52}Cu_{32}Ni_6Al_{10}$ and Wf/$(Zr_{52}Cu_{32}Ni_6Al_{10})_{98}Nb_2$ exhibit similar mechanical properties, and similarly, Wp/$Zr_{52}Cu_{32}Ni_6Al_{10}$ and Wp/$(Zr_{52}Cu_{32}Ni_6Al_{10})_{98}Nb_2$ also demonstrate comparable mechanical properties. Therefore, it can be inferred that the density of shear bands significantly influences the mechanical properties of the composite materials [27]. In general, the denser the shear bands on the amorphous alloy matrix, the better the corresponding plasticity of the composite materials.

4 Conclusions

(1) At the soaking temperature of 1,010 °C, all three types of amorphous alloys exhibit good wettability with tungsten materials. Furthermore, $(Zr_{52}Cu_{32}Ni_6Al_{10})_{98}Be_2$ demonstrates the best wettability with tungsten, while there is not a significant difference in the wettability between $Zr_{52}Cu_{32}Ni_6Al_{10}$ and $(Zr_{52}Cu_{32}Ni_6Al_{10})_{98}Nb_2$ with tungsten.

(2) The cross-sectional microstructures of Wf/$Zr_{52}Cu_{32}Ni_6Al_{10}$, Wp/$Zr_{52}Cu_{32}Ni_6Al_{10}$, Wf/$(Zr_{52}Cu_{32}Ni_6Al_{10})_{98}Be_2$ and Wp/$(Zr_{52}Cu_{32}Ni_6Al_{10})_{98}Be_2$ show the presence of W-Zr phase. The cross-sectional microstructures of Wf/$(Zr_{52}Cu_{32}Ni_6Al_{10})_{98}Nb_2$ and Wp/$(Zr_{52}Cu_{32}Ni_6Al_{10})_{98}Nb_2$ do not exhibit the W-Zr phase.

(3) The tungsten reinforcement significantly impacts the mechanical performance of the composite material. Tungsten
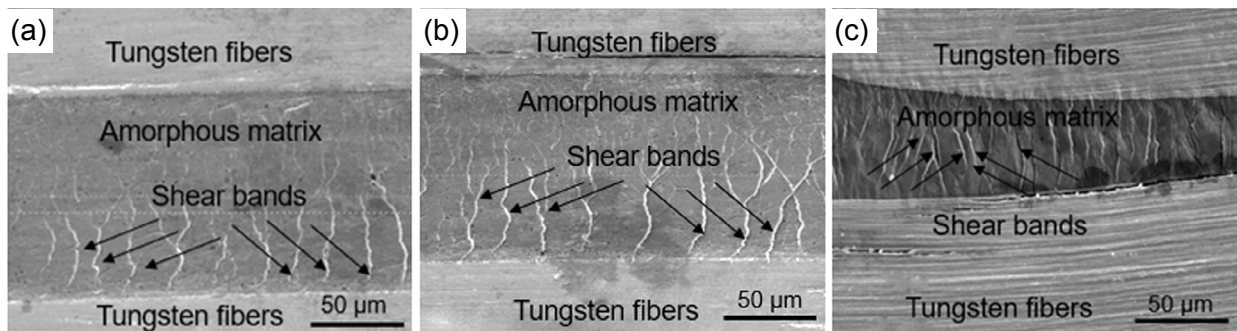

Fig. 9: Morphology of shear fracture surfaces of tungsten fiber-reinforced: (a) Wf/$Zr_{52}Cu_{32}Ni_6Al_{10}$; (b) Wf/$(Zr_{52}Cu_{32}Ni_6Al_{10})_{98}Nb_2$; (c) Wf/$(Zr_{52}Cu_{32}Ni_6Al_{10})_{98}Be_2$
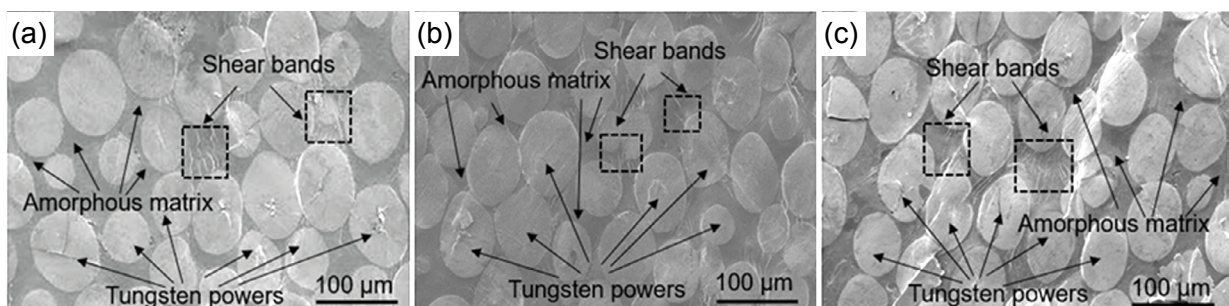

Fig. 10: Morphology of shear fracture surfaces of tungsten powder-reinforced: (a) Wp/$Zr_{52}Cu_{32}Ni_6Al_{10}$; (b) Wp/$(Zr_{52}Cu_{32}Ni_6Al_{10})_{98}Nb_2$; (c) Wp/$(Zr_{52}Cu_{32}Ni_6Al_{10})_{98}Be_2$

fiber-reinforced composite has a yield strength of over 2,400 MPa and a plasticity of over 3.9%. However, tungsten powder-reinforced composite has a yield strength of over 2,700 MPa and a plasticity of over 30%.

(4)) The XRD patterns of both types of composites reveal distinct diffraction peaks associated with the tungsten fiber and tungsten powder reinforcements. Additionally, the presence of diffraction peaks corresponding to W-Zr phase and the phases resulting from partial crystallization of the amorphous matrix is observed.

(5) Tungsten fiber-reinforced amorphous composite materials exhibit a longitudinal splitting mode, which can be further classified into two types: fracture through tungsten fibers and along the amorphous matrix. While, tungsten powder-reinforced amorphous composite materials demonstrate a shear fracture mode.

(6) The denser the shear bands on the amorphous matrix of the composite materials, the better its mechanical properties.

Acknowledgments

Conflict of interest

Authors declare that they have no conflict of interest.

References

[1] Inoue A, Takeuchi A. Recent development and application products of bulk glassy alloys. Acta Materialia, 2011, 59(6): 2243–2267.

[2] Sopu D, Albe K, Eckert J. Metallic glass nanolaminates with shape memory alloys. Acta Materialia, 2018, 159: 344–351.

[3] Klement W, Willens R H, Duwez P. Non-crystalline structure in solidified gold-silicon alloys. Nature, 1960, 187(4740): 869–870.

[4] Wang W H, Dong C, Shek C H. Bulk metallic glasses. Materials Science & Engineering: R, 2004, 44(2–3): 45–89.

[5] Pauly S, Gorantla S, Wang G, et al. Transformation-mediated ductility in CuZr-based bulk metallic glasses. Nature Materials, 2010, 9(6): 473–477.

[6] Trexler M M, Thadhani N N. Mechanical properties of bulk metallic glasses progress in materials. Science, 2010, 55(8): 759–839.

[7] Inoue A. Stabilization of metallic supercooled liquid and bulk amorphous alloys. Acta Materialia, 2000, 48(1): 279–306.

[8] Argon A S. Plastic-deformation in metallic glasses. Acta Metallurgica, 1979, 27(1): 47–58.

[9] Du W, Yan Z, Wu, Y, et al. Conventional and novel fabrication of magnesium matrix composites. Rare Metal Materials and Engineering, 2009, 38(3): 559–564.

[10] Mukai T, Nieh T G, Kawamura Y, et al. Effect of strain rate on compressive behavior of a $Pd_{40}Ni_{40}P_{20}$ bulk metallic glass. Intermetallics, 2002, 10(11–12): 1071–1077.

[11] Jia H, Wang G, Chen S, et al. Fatigue and fracture behavior of bulk metallic glasses and their composites. Progress in Materials Science, 2018, 98: 168–248.

[12] Leng Y, Courtney T H. Multiple shear band formation in metallic glasses in composites. Journal of Materials Science, 1991, 26(3): 588–592.

[13] Cytron S J A. Metallic glass-metal matrix composite. Journal of Materials Science Letters, 1982, 1(5): 211–213.

[14] Zhang Z F, He G, Zhang H, et al. Rotation mechanism of shear fracture induced by high plasticity in Ti-based nano-structured composites containing ductile dendrites. Scripta Materialia, 2005, 52(9): 945–949.

[15] Zhang X Q, Wang L, Xue Y F, et al. Effect of the metallic glass volume fraction on the mechanical properties of Zr-based metallic glass reinforced with porous W composite. Materials Science and Engineering: A, 2013, 561: 152–158.

[16] Deng S T, Diao H, Chen Y L, et al. Metallic glass fiber-reinforced Zr-based bulk metallic glass. Scripta Materialia, 2011, 64(1): 85–88.

[17] Wang H, Zhang H F, Hu Z Q. Tungsten fibre reinforced Zr-based bulk metallic glass composites. Materials and Manufacturing Processes, 2007, 22(5–6): 687–691.

[18] Qiu K Q, Suo Z Y, Ren Y L, et al. Observation of shear bands formation on tungsten fiber-reinforced Zr-based bulk metallic glass matrix composite. Journal of Materials Research, 2007, 22(2): 551–554.

[19] Zhang B, Fu H M, Zhang H F, et al. Synthesis and property of short tungsten fiber/Zr-based metallic glass composite. Materials Science and Technology, 2019, 35(11): 1347–1354.

[20] Dandliker R B, Conner R D, Johnson W L. Melt infiltration casting of bulk metallic-glass matrix composites. Journal of Materials Research, 1998, 13(10): 2896–2901.

[21] Takeuchi A, Inoue A. Classification of bulk metallic glasses by atomic size difference, heat of mixing and period of constituent elements and its application to characterization of the main alloying element. Materials Transactions, 2005, 46(12): 2817–2829.

[22] Li Z K, Fu H M, Sha P F, et al. Atomic interaction mechanism for designing the interface of W/Zr-based bulk metallic glass composites. Scientific Reports, 2015, 5: 254–260.

[23] Liu N, Ma G F, Zhang H F, et al. Wetting behavior of Zr-based bulk metallic glasses on W substrate. Materials Letters, 2008, 62(17–18): 3195–3197.

[24] Zhu Z W, Zhang H F, Hu Z Q, et al. Ta-particulate reinforced Zr-based bulk metallic glass matrix composite with tensile plasticity. Scripta Materialia, 2010, 62(5): 278–281.

[25] Dragoi D, Üstündag E, Clausen B, et al. Investigation of thermal residual stresses in tungsten-fiber/bulk metallic glass matrix composites. Scripta Materialia, 2001, 45(2): 245–252.

[26] Hui X, Dong W, Chen G L, et al. Formation, microstructure and properties of long-period order structure reinforced Mg-based bulk metallic glass composites. Acta Materialia, 2007, 55(3): 907–920.

[27] He G, Eckert J, Löser W, et al. Novel Ti-base nanostructure-dendrite composite with enhanced plasticity. Nature Materials, 2003, 2(1): 33–37.